Ionization disequilibrium in K- and L-shell ions

D. T. Bishel, ^{1,2} E. V. Marley, ³ M. B. Schneider, ³ D. A. Liedahl, ³ R. F. Heeter, ³ M. E. Foord, ³ G. E. Kemp, ³ Y. Frank, ³ J. A. Emig, ³ G. Pérez-Callejo, ⁴ P. M. Nilson, ⁵ D. A. Chin, ^{1,2} J. R. Rygg, ^{1,2,6} and G. W. Collins ^{1,2,6}

1) Department of Physics and Astronomy, University of Rochester

³⁾Lawrence Livermore National Laboratory

(*Electronic mail: dbishel@ur.rochester.edu)

(Dated: 31 January 2023)

Time-gated Sc K-shell and Ge L-shell spectra are presented from a range of characterized thermodynamic states spanning ion densities $10^{19}~\text{cm}^{-3} < n_i < 10^{20}~\text{cm}^{-3}$ and plasma temperature $T_e \approx 2000~\text{eV}$. For $5 \times 10^{19}~\text{cm}^{-3} < n_i < 10^{20}~\text{cm}^{-3}$ and $1200~\text{eV} < T_e < 1700~\text{eV}$, the Sc and Ge x-ray emission spectra are consistent with steady-state calculations from the modern atomic kinetics model SCRAM. At the lower ion densities achieved through plasma expansion, however, the model calculations require different plasma temperatures to reproduce the observed Ge and Sc spectra. We determine this to be due to ionization disequilibrium of the Sc and possibly the Ge, since the ionization time scales exceed the hydrodynamic time scale as the inferred temperatures diverge.

I. INTRODUCTION

Accurate models of atomic spectra enable the robust design of systems where energy transport by the atomic spectra is important, including stellar ejecta and Au ablation plasmas in inertial fusion hohlraums. The accuracy of model calculations can only be verified by comparison to experimental spectra observed from a source with a characterized thermodynamic state.

The problem of model verification is particularly pronounced for non-local-thermodynamic-equilibrium (non-LTE) spectral models of multiple-electron ions. The complete set of atomic states increases exponentially with atomic number *Z* and exceeds current computational capabilities even for modest *Z*. Truncating schemes are thus employed to keep calculations tractable.² These approximations inherently introduce uncertainty into the models. Recent international workshops have shown variation among different non-LTE codes when modeling spectra from open-shell configurations.^{3,4}

Though non-LTE spectra have been studied at high-energydensity (HED) facilities for decades, the creation and characterization of a plasma suitable for model verifiaction has proven to be difficult. Few datasets exist in the literature as a consequence. More recently, the buried-layer platform, in which a submicron witness layer is centrally buried in a low-Z tamper, has been deployed at high-power-laser facilities to create a homogeneous, expanding plasma at non-LTE conditions.^{5–9} Both sides of the disk-like target are irradiated by a high-power laser to rapidly heat and expand the sample. The centrally buried layer is collisionally confined in the radial direction by the surrounding low-Z tamp, mitigating radial gradients and resulting in uniaxial expansion along the target normal. Axial gradients (along the expansion axis) in temperature are reduced once the plasma expands to subcritical densities since laser energy deposition is nearly uniform in the underdense plasma. ^{10,11} Axial tamping helps homogenize the density within the witness layer and slows the rate of expansion. Creation of uniform conditions simplifies comparison between observed spectra and spectral model calculations because only a single thermodynamic state needs to be considered.

However, there is a risk of ionization disequilibrium in the expanding plasma. When the thermodynamic time scale is faster than the ionization equilibration time scale, the ionization state will depart from its steady-state ("equilibrium") distribution and must be treated with a time-dependent calculation. This time-dependent ionization manifests in the measured spectrum. Using such time-dependent spectra to validate steady-state calculations is improper and will give false results. Previous buried-layer and "spot-spectroscopy" (where the material of interest is tamped radially but not in the direction of expansion, leading to large axial gradients) studies have explored time-dependent ionization kinetics, but the conclusions have been varied. The threshold for steady-state ionization is a function of plasma temperature T_e, ion density n_i, nuclear charge, and ionization state through the ionization and thermodynamic time scales. Due to this multivariate dependence, it is not contradictory that previous publications have reached different conclusions of timedependence for the particular target geometry and elements considered. Some studies have argued for the sufficiency of a steady state, 10 while others demonstrated the need for timedependent ionization, 12 and still others indicated the presence of regions of steady-state and of time-dependent ionization within the same plasma.¹³ Whether or not the ionization is time-dependent is idiosyncratic to the given platform. The potential for time-dependence must be considered when using the ionization state as a thermodynamic diagnostic. To our knowledge, no observation of K-shell disequilibrium in axially-tamped buried-layer targets has been published.

We present Sc K-shell and Ge L-shell spectra from a characterized buried-layer plasma. L-shell spectroscopy was recently proposed by Marley *et al.* as a thermodynamic diagnostic that is more sensitive to the plasma conditions than traditional K-shell measurements.¹⁴ Additionally, the two species

²⁾Laboratory for Laser Energetics, University of Rochester

⁴⁾Deparamento de Física Teórica, Atómica y Óptica, Universidad de Valladolid, Spain

⁵⁾Laboratory for Laser Energetics, University of Rochester.

⁶⁾ Department of Mechanical Energy, University of Rochester

have different ionization equilibration time scales due to their different nuclear charge and ionization state. By fitting each spectrum with steady-state calculations from the atomic kinetics model SCRAM, ¹⁵ an ionization temperature T_Z of each species can be inferred. For each species whose ionization is in thermal equilibrium with the circumfluent plasma, ¹⁶ $T_Z = T_e$. Thus, spectra from the two species will test the spectral model more stringently than a single spectrum, while also providing a means to determine if the ionization distributions have attained a steady state.

The paper is organized as follows. In Sec. II, we describe the experimental geometry and the suite of diagnostics used. Constraints on the plasma conditions are derived in Sec. III, where we outline the data reduction and analysis of each diagnostic. In Sec. IV A, we demonstrate that the Sc and Ge spectra obtained early during the expansion show phenomenal agreement with steady-state calculations constrained by the measured ion density, while spectra obtained once the plasma has expanded to $n_i \approx 10^{19} \ cm^{-3}$ are not reproduced by steady-state calculations. In Sec. IV B, we demonstrate that ionization time scales exceed the hydrodynamic time scale, indicating that the Sc ionization has departed from its steady state distribution. After this time, the Sc spectra must be represented by time-dependent calculations.

II. EXPERIMENTAL CONFIGURATION

Targets consisted of a 250-\mu m-diam Ge:Sc spot centrally buried in a 1-mm-radius, $10-\mu$ m-thick Be tamp (see Fig. 1). The buried layer consisted of sequentially deposited layers of 300 Å Sc, 600 Å Ge, and 300 Å Sc. Targets were irradiated from both sides with a total of 7.5 ± 0.4 kJ laser energy on target over 3.5 ns using a constant intensity drive. All measurements were obtained during the laser drive. Beams were propagated through focus to achieve an approximately 600- μ m-diam spot size at target chamber center (TCC), providing a drive intensity of 10¹⁴ W/cm² on each face of the sample. The high-intensity laser ablates, burns through, and causes the entire target package to expand along the target normal. The buried layer is kept thin to mitigate axial gradients and maintain uniform plasma conditions throughout the Ge:Sc layer. Targets fabricated without a buried layer were also shot to determine the contribution of the Be tamp and its impurities to the data.

An array of 16 pinholes was coupled to a four-strip x-ray framing camera¹⁷ with a 50-ps integration window to capture time-resolved x-ray images of the plasma emission. Two such cameras were deployed looking nearly parallel and perpendicular to the target normal yielding face-on and side-on views, respectively, of the expansion. These orthogonal views of the x-ray emission of the Ge and Sc are used to estimate the average ion density during expansion.

Sc K-shell and Ge L-shell spectra are obtained simultaneously with the x-ray images. The spectra were collected by separate multipurpose spectrometers (MSPECs), ^{18–20} timegated by x-ray framing cameras with a 200-ps integration window, and recorded on Kodak T-Max 400 film. For conve-

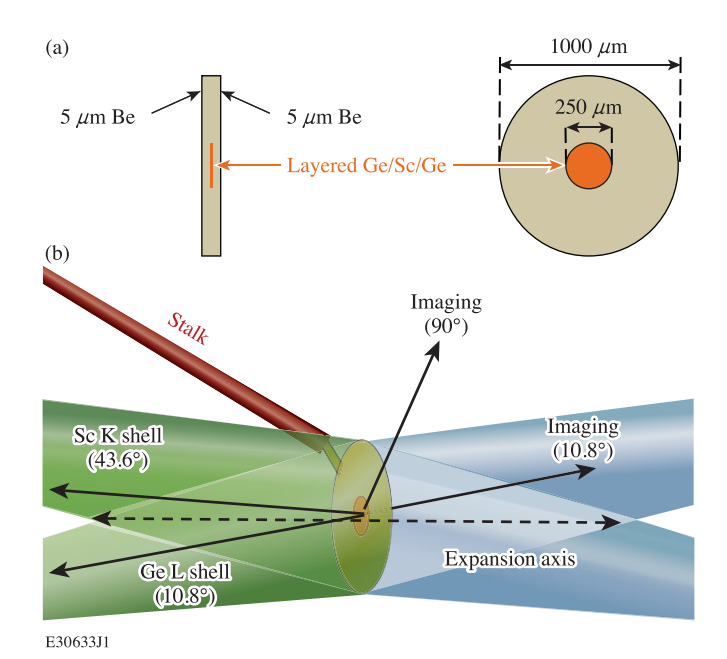


FIG. 1. (a) Cross-sectional views of the target, side-on (left) and face-on (right). The Ge:Sc layer is centrally buried within a $10\text{-}\mu\text{m}$ -thick Be tamp and consisted of 300 Å Sc, 600 Å Ge, and 300 Å Sc. (b) Experimental geometry showing the two-sided irradiation of the target and lines of sight of the imaging and spectroscopic diagnostics. Angles of each diagnostic are shown with respect to the expansion axis.

nience, we will refer to the two spectrometers according to the species they were configured to observe, i.e. the Sc spectrometer and the Ge spectrometer. The steady-state mean ionization state \bar{Z} of each element at relevant conditions is shown in Fig. 2. Above 1 keV, the Sc \bar{Z} is a function of T_e only, while Ge's \bar{Z} is a function of both T_e and n_i . Furthermore, the K-shell emission spectrum of Sc changes dramatically with increasing temperature (Fig. 3), making Sc a compelling temperature diagnostic.

III. DATA ANALYSIS

A. X-ray Images

An example of the orthogonal x-ray images is shown in Fig. 4. After subtracting emission from the images due to the Be tamp, the height of the expansion visible in the side-on images is inferred as the full-width at half-maximum (FWHM) of a Gaussian profile. An azimuthally averaged diameter is inferred from the face-on images as the FWHM of a fourth-order super-Gaussian. The Ge and Sc are assumed to homogeneously occupy a cylindrical volume given by the measured height and diameter. The average ion density is calculated from this volume and the characterized initial mass of the buried layer assuming conservation of particles. Due to the high signal-to-noise ratio in the images, the statistical uncertainty in n_i from fitting the emission volume produces a fractional random uncertainty of $\leq 2.5\%$. Metrology of the initial

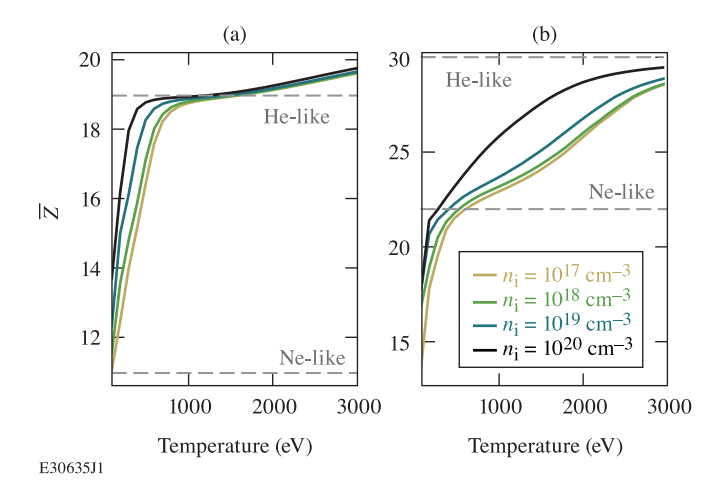


FIG. 2. Mean ionization state \bar{Z} of (a) Sc and (b) Ge plotted versus temperature for various densities. The \bar{Z} of Sc varies little with density and can be used as a temperature diagnostic. Interpretation of the \bar{Z} of Ge requires knowledge of density for $n_i > 10^{18}$ cm⁻³. The He-like and Ne-like states for each species are plotted as the dashed gray lines for reference.

buried-layer mass gives a fractional systematic uncertainty in n_i of 11%.

Extracting ion density from self-emission images has been previously validated against spectroscopic line ratios of Fe:V buried-layer targets. 21,22 In that work, radiative-transfer calculations were used to predict the enhancement of the Helike resonance line $(^1S-^1P^0)$ over the intercombination line $(^1S-^3P^0)$ as a function of target viewing angle and aspect ratio of the expanding buried layer. The relative enhancement between spectra obtained from face-on and side-on views of the layer required an ion density consistent with that measured by self-emission images.

B. Sc K-shell Spectra

At the measured n_i , an accurate and complete model should describe the spectra of both species with the same set of T_e or a single T_e if the plasma is uniform. Together with the x-ray images, we use the Sc and Ge spectra to benchmark the non-LTE atomic kinetics model SCRAM. ¹⁵

Sc K-shell spectra are processed by accounting for the spectral sensitivity of the various spectrometer components according to Marrs $et~al.^{20}$ Raw and processed data are shown in Fig. 5. Notable lines in the Sc spectra include the H-like series 1s-np, the He-like series $1s^2-1s~np$, and the Li-like satellites $1s^2n\ell-1s2p~n\ell$ on the low-energy side of the He_{α} complex $1s^2-1s2p$. We infer the ionization temperature T_Z of the Sc by fitting the observed Sc K-shell spectra with spectra calculated by SCRAM assuming steady-state populations. When the thermodynamic time scales $\tau_{hydro} = \left(\frac{1}{n_i}\frac{dn_i}{dt}\right)^{-1}$ and $\tau_{th} = \left(\frac{1}{T_e}\frac{dT_e}{dt}\right)^{-1}$ exceed the time scale for ionization, the ionization state of species X will have sufficient time to respond to changes in the local thermodynamic state, and $T_Z^X = T_e$.

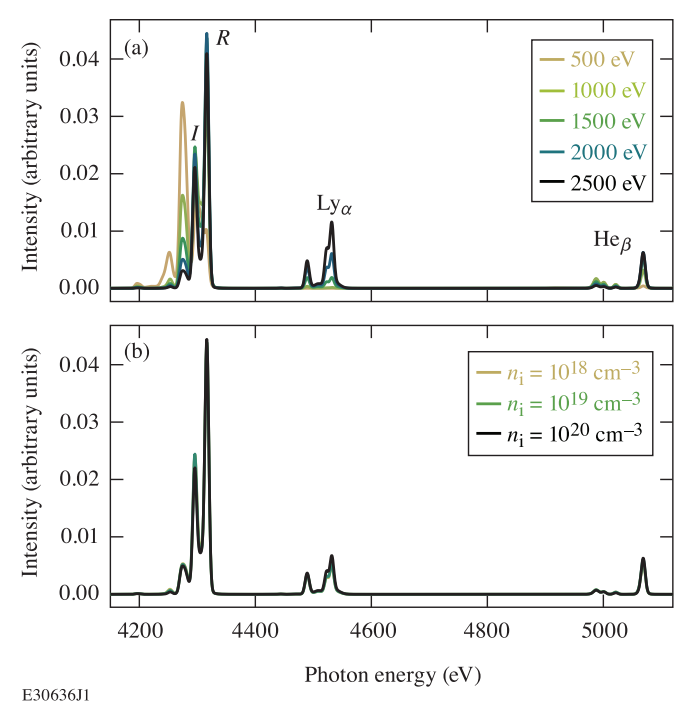


FIG. 3. Portion of steady-state Sc K-shell spectrum calculated by SCRAM (a) for various temperatures at $n_i = 5 \times 10^{19}~{\rm cm}^{-3}$ and (b) for various ion densities at $T_e = 2000~{\rm eV}$. Labels denote the Ly $_\alpha$ and He $_\beta$ complexes, and the resonance ($^1S - ^1P^0$, R) and intercombination ($^1S - ^3P^0$, I) lines of the He $_\alpha$ complex. The represented conditions bracket those achieved in the experiments. The steady-state Sc spectrum changes almost exclusively with temperature, motivating its use as a temperature diagnostic.

The He_{α} , He_{β} , and Ly_{α} complexes including satellite lines are included in the fit, and the intervening continuum regions are ignored. Studies by Pérez-Callejo *et al.* demonstrated the importance of anisotropy effects on He-like line ratios when the resonance line is not optically thin. ^{21,23} Optical depths of all lines in this study are estimated from *SCRAM* across the range of temperatures and densities considered, and are found to be optically thin; additional details can be found in Sec. IV.

In the following analysis, we find that temperature gradients are not necessary to describe the Sc spectra. A set of single-temperature steady-state spectra were generated from SCRAM and treated as a set of basis vectors to reproduce the observed spectra. Assuming the plasma is optically thin and consists of a distribution of temperatures, the observed spectrum S_x is modeled as a linear sum of the generated spectra $S(T_j, \bar{\mathbf{n_i}})$, each with an unknown abundance (or discretized differential emission measure) a_j :

$$S_x = \sum_j a_j S(T_j, \, \bar{\mathbf{n}}_i), \tag{1}$$

where $\bar{n_i}$ is the average density during the 200-ps integration of the corresponding framing camera. The Sc K-shell spectra are negligibly sensitive to density changes of a factor of 10 (see Fig. 3), such that either small errors or gradients in the density measurement affect the inferred temperature by at

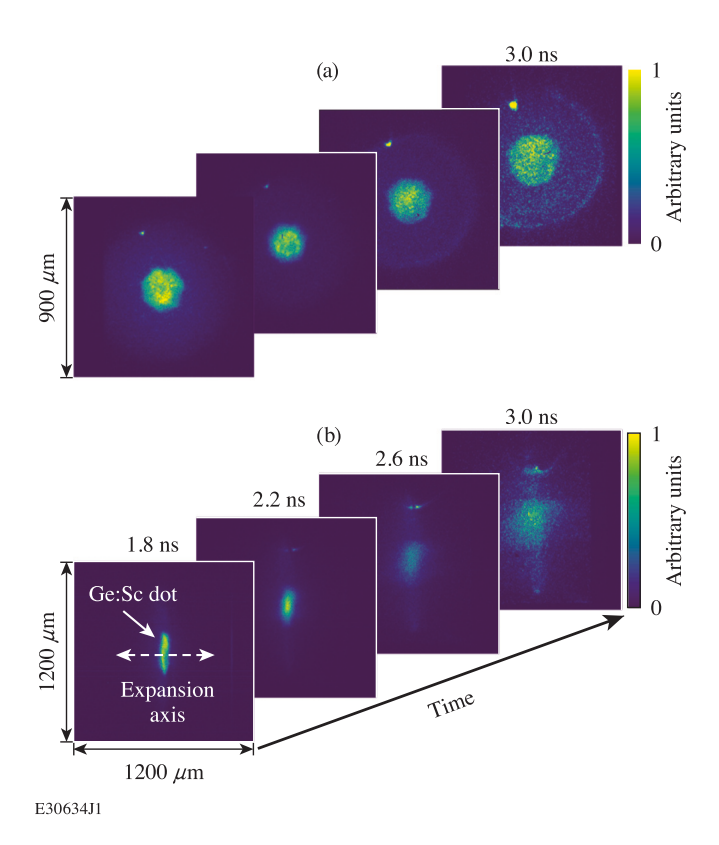


FIG. 4. (a) Face-on and (b) side-on images obtained throughout the expansion phase after the laser burned through the Ge:Sc layer. Spatial scales are noted in the first image of each row, and times are listed above each image. The Ge:Sc layer is visible inside the diffuse emission of the surrounding Be tamper. The Ge:Sc layer expands horizontally in the side-on images, revealing a uniaxial expansion.

most 100 eV (and likely much less). To conserve the number of Ge and Sc atoms in the system, $\sum_j a_j = 1$. The spectral fit is then found by determining the relative abundance a_j of each temperature component T_j .

The inferred abundance distributions that best fit each spectrum assign all of the abundance into a single temperature or two neighboring temperatures. Such unimodal and narrow abundance distributions indicate that each spectrum is well-described by a single-temperature plasma. Fig. 5 reveals the ability of a single-temperature spectrum to reproduce the data. For the remainder of the manuscript, the plasma will be treated as single-temperature. χ^2 uncertainty analysis assuming a uniform plasma suggests a 10% uncertainty in the inferred temperature. Synthetic spectra at 1700 eV and 2200 eV ($\approx \pm 10\%$ of the best-fit temperature) are overlayed in Fig. 5 to demonstrate the sensitivity of this diagnostic to temperature. This analysis is repeated for Sc spectra obtained at multiple times throughout the experiment to determine $T_{\rm c}^{\rm SC}(t)$.

Combining the ion density and temperature analyses, we can reconstruct the evolution of the buried layer through $T_Z - n_i$ space (Fig. 6). Acquisition of (T_Z, n_i) begins at 1.5 ns, after the laser has ablated through the Be tamper and into the buried layer. Arrival of the ablation front at the Ge:Sc layer is signaled both by the bright emission from the Ge:Sc

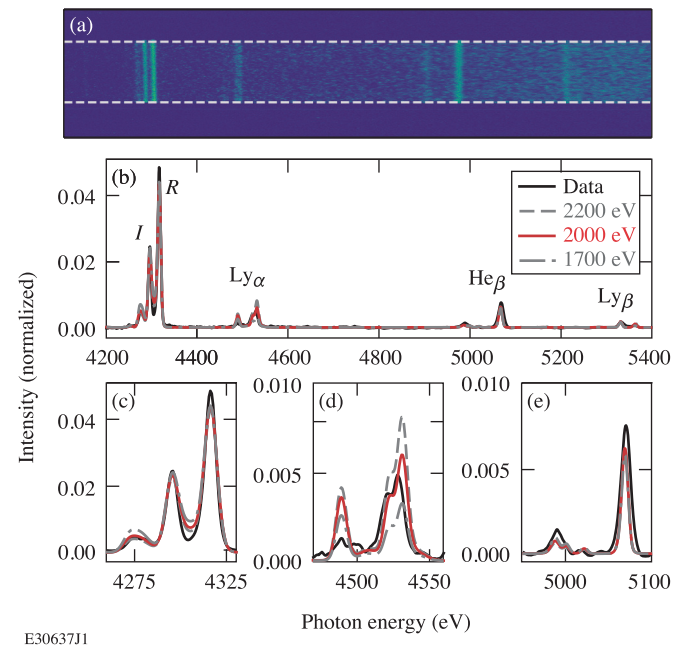


FIG. 5. (a) Raw data and (b) unfolded spectrum (black) of the Sc K-shell emission at 2.6 ns and plotted on the same photon energy axis. In (a), the vertical extent of the framing camera strip is demarcated by the dashed white lines. Magnified views of various features are shown in (c) – (e). See caption of Fig. 3 for label definitions. Synthetic spectra at the specified temperatures are also plotted, indicating sensitivity to temperature, particularly of the Ly $_{\alpha}$ peak and the Li-like satellites of He $_{\alpha}$ (transitions of the type $1s^2n\ell-1s2p\ n\ell$). T^{Sc}_Z = 2000 eV was deemed to be the best fit by a least squares approach ($\chi^2_{\min} = 6.3$). The remaining temperatures were chosen for having $\chi^2 > \chi^2_{\min} + 1\ (\chi^2_{1700} = 7.7,\ \chi^2_{2200} = 7.3)$. The deviation of χ^2_{\min} from 1 is due in part to imperfections in the dispersion relation. The intensity of the He-like satellite of Ly $_{\alpha}$ shown in (d) below hv = 4500 eV is overpredicted by all temperatures.

layer visible in the x-ray images and by the increasing ionization evident in the spectra. From 1.5 to 2.5 ns, direct illumination by the laser causes the buried layer to rapidly heat and expand. By 2.5 ns, a uniform plasma temperature is established within the buried layer when deposition of laser energy and conduction from the surrounding hot Be reservoir are balanced by mechanical losses from expansion and radiative losses from emission, consistent with previous modeling and experiments^{10,11} of buried-layer targets. Two-dimensional simulations of similar experiments indicate a high degree of radial and axial uniformity after the laser burns through the buried layer.²⁴ Meanwhile, the density continues to decrease as the buried layer expands into the surrounding Be tamp. An accelerated decrease in density at 2.5 ns (Fig. 6) is caused by radial expansion as the pressure equilibrates between the expanding Ge:Sc region and the surrounding Be.²⁴ This expansion follows a radially inward-propagating density perturbation launched by an increased pressure on the sides of the Ge:Sc layer once the laser burns through the Be tamp but has yet to fully burn through the Ge:Sc. This density perturbation leads to a slight enhancement in x-ray emission, visible as the

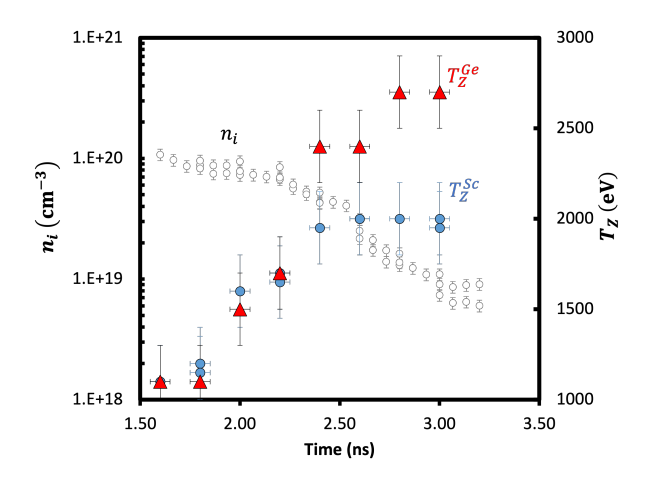


FIG. 6. Ion density (open circles) inferred from the emitting volume of the expanding targets, and ionization temperatures of Ge (red) and Sc (blue) inferred from their respective spectra. Sc and Ge spectral measurements coincide with temperature data. Conditions of multiple shots are shown to demonstrate the repeatability of the plasma conditions.

faint ring of emission inside the Ge:Sc layer at 2.2 ns. Because emissivity scales with n_e^2 , the density perturbation is estimated from the ratio between the signal in the ring to the signal interior to the ring to be less than 5%. The radial expansion is visible in the face-on images of Fig. 4.

C. Ge L-shell Spectra

Ge L-shell spectra were collected and unfolded in the same manner as the Sc spectra. The unfolded spectra are shown as black traces in Fig. 7, and identified lines are listed in Table I. A line emission feature at 1570 eV has been removed from the Ge spectra, identified as He_{α} emission from Ar (hv = 3140 eV) in the Be tamper that is reflected from the spectrometer crystal in the second order. Ar contaminated the Be tamper during the coating process. Observation of Helike Ar lines in the first order on the Sc spectrometer (not depicted) confirms that Ar is present in targets with and without the Ge:Sc buried layer. The 1570-eV line persists in the Ge spectrometer in Be-only targets. Furthermore, the structure of this line does not evolve as the Ge:Sc layer is heated, indicating that the contaminant must lie in the already-heated tamper. Other Ar lines, including Ly α , lie within range of the Ge spectrometer and do not contribute substantially to the spectrum.

The centroid of the Ge L-shell spectra is a measure of ionization since ionization increases the energy difference between the orbitals (predominantly 3d and 2p) that participate in the observed transitions. The shift of this centroid to higher photon energy indicates a charge-state distribution that increases during the early phase of the experiment (t < 2.4 ns) and plateaus in the late phase (t > 2.4 ns). This observed

trend in ionization qualitatively follows the temperature inferred from Sc.

IV. BENCHMARKING THE ATOMIC KINETICS MODEL

A. Steady-state calculations

We now consider the consistency of the atomic model by calculating steady-state Ge spectra given the n_i measured from the x-ray images and assuming $T_e = T_Z^{Sc}$. The steady-state calculations are compared to the unfolded spectra in Fig. 7. It is stressed that these are not fits to the Ge spectra, but rather use the experimental observables of T_Z^{Sc} and n_i as inputs to SCRAM. At the earlier times (1.8 to 2.2 ns), the predicted envelope agrees with the observed spectra, and line positions are accurately reproduced, most notably the distinct Be- and Li-like lines above hv = 1700 eV that emerge at 2.2 ns. The kinetics model assigns consistent ionization temperatures to the Ge and Sc during the early expansion phase of the plasma. It is likely that both Sc and Ge have equilibrated to the local plasma conditions, and $T_Z^{Sc} = T_Z^{Ge} = T_e$.

After 2.2 ns, the Ge spectra calculated at T_Z^{Sc} are in stark contrast to the observed spectra. Once T_Z^{Sc} and the observed Ge ionization plateau, the *SCRAM*-predicted Ge ionization distribution recombines in response to the decreasing density of the expanding plasma. Consequently, the strong $3d^1 \rightarrow 2p^1$ Li-like lines at 1730.6 eV and 1766.0 eV in the synthetic spectra decrease in intensity as the Li-like population decreases, and the envelope of the emission shifts to lower photon energies as less-ionized charge states are populated. In the observed spectra, however, the Li-like lines persist, and the emission envelope does not shift.

The late-time Ge and Sc spectra cannot be modeled with steady-state calculations at a single set of plasma conditions. In the preceding analysis, we have generated synthetic Ge L-shell spectra at $T_e = T_Z^{Sc}$, and we find disagreement with the observed Ge spectra. We can instead identify temperatures T_Z^{Ge} that describe the Ge spectra (see Fig. 7 for fits and Fig. 6 for $T_Z^{Ge}(t)$). Uncertainty in T_Z^{Ge} is conservatively estimated to be 200 eV. Even accounting for uncertainties, $T_Z^{Ge} > T_Z^{Sc}$ at late times. We note that Sc spectra generated at T_Z^{Ge} substantially overpredict the observed intensity of the Ly_{α} feature. We are unable to accurately reproduce both the Sc and Ge late-time spectra with the same set of conditions while assuming a steady-state ionization.

We have investigated the effects of the assumptions made in this analysis to confirm that the discrepancy in T_Z is not artificially introduced by the assumptions. We discuss these below.

The absolute density n_i does not affect our conclusions. We have inferred density from the volume of the emitting plasma. Images clearly indicate that the plasma is expanding, so the density must be decreasing throughout the measurements. SCRAM predicts recombination with decreasing density in the range of 10^{17} to 10^{22} ions/cm³. As such, a different $n_i(t)$ (with the requirement $\frac{dn_i}{dt} < 0$) would still yield recombination.

TABLE I. Transition energies of observed lines from B-, Be-, and Li-like Ge ions as reported by *SCRAM*. Strong lines visible in the late time Ge L-shell spectra predominantly are due to $3d \rightarrow 2p$ transitions.

Isoelectronic	Upper	Lower	Transition
sequence	configuration	configuration	energy (eV)
Li	$3s^1$	$2p^1$	1691.7
Li	$3d^{1}$	$2p^{1}$	1730.6
Li	$3d^1$	$2p^{1}$	1766.0
Be	$2s^{1}3d^{1}$	$2s^{1}2p^{1}$	1666.5
Be	$2p^{1}3d^{1}$	$2p^{2}$	1669.5
Be	$2p^{1}3d^{1}$	$2p^2$	1679.4
Be	$2p^{1}3d^{1}$	$2p^{2}$	1681.6
Be	$2s^{1}3d^{1}$	$2s^{1}2p^{1}$	1698.6
Be	$2p^{1}3d^{1}$	$2p^{2}$	1705.1
В	$2p^23d^1$	$2p^{3}$	1614.7
В	$2p^23d^1$	$2p^{3}$	1616.0
В	$2s^12p^13d^1$	$2s^{1}2p^{2}$	1635.9
В	$2p^23d^1$	$2p^3$	1654.4

nation in the synthetic spectra. On the contrary, the observed spectra do not change appreciably after 2.2 ns, indicating that the true ionization of Ge does not change in response to the decreasing density. We conclude that an error in the absolute density would not cause the observed inconsistency.

Optical depth $\tau_V = \rho \kappa_V L$ is insufficient to modify the line ratios. At 2.0 ns the extinction length $(\rho \kappa_V)^{-1}$ for the Sc Helike resonance line is greater than 3000 μ m and that for the

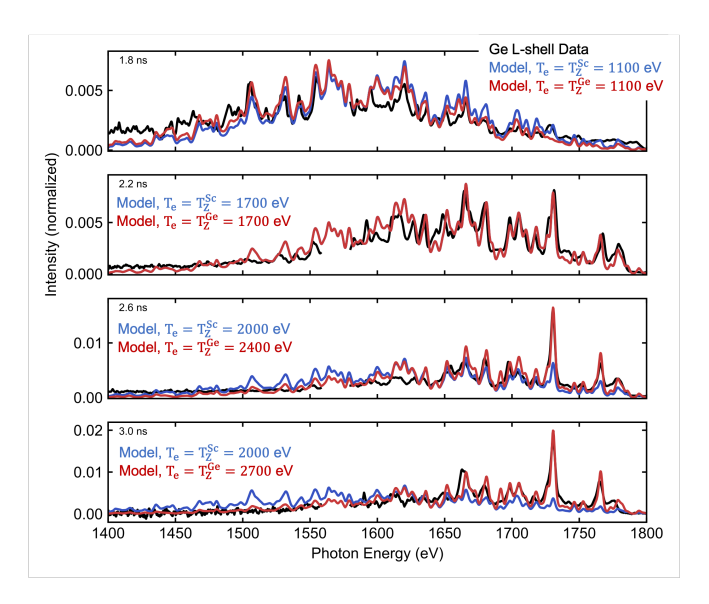


FIG. 7. Observed Ge L-shell spectra (black) and steady-state SCRAM calculations along the inferred temperature (T_Z^{Sc} in blue and T_Z^{Ge} in red) and density trajectories shown in Fig. 6. All spectra are normalized to the integrated signal in the energy range displayed. Numerical labels indicate the isoelectronic sequence producing prominent features (3 = Li-like, 4 = Be-like, 5 = B-like). Time steps are noted in each figure in the upper left corner. Steady-state calculations at T_Z^{Sc} fail to reproduce the Ge spectra after t = 2.4 ns.

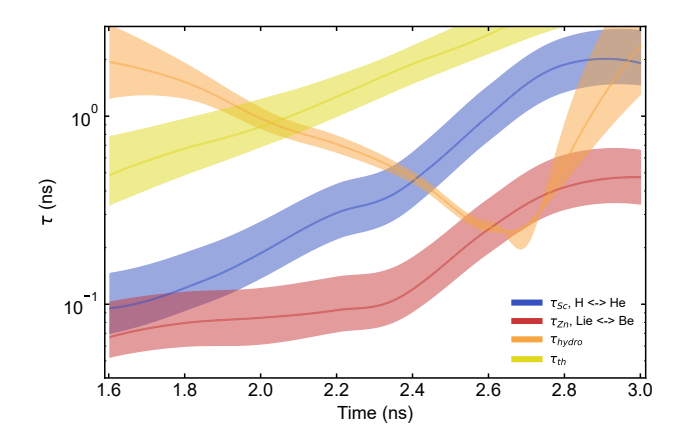


FIG. 8. Ionization equilibration time scales in the two-ion-state model of Sc He- to H-like (blue) and Zn Be- to Li-like as a proxy for Ge (red), hydrodynamic time scale τ_{hydro} (orange), thermal time scale τ_{th} (yellow), and associated 90% HDI's evaluated for T_Z^{Ge} . τ_{hydro} crosses τ_{Sc} between 2.3 and 2.5 ns, consistent with when $T_Z^{Se} \neq T_Z^{Ge}$.

entire Ge spectrum is greater than 1000 μ m. Both extinction lengths increase as the plasma density decreases. The height and radius of the Ge:Sc layer at this time are 50 μ m and 125 μ m, respectively. Accounting for the viewing angles of the Ge (10.8°) and Sc (43.6°) spectrometers, the chord-integrated depth seen by the Ge spectrometer is 50 μ m and that of the Sc spectrometer is 350 μ m. Even at the latest times when the plasma has expanded to a height of 400 μ m and a radius of 160 μ m, the extinction lengths exceed the chord-integrated depth of the plasma, indicating that τ_{v} << 1 and optical depth effects do not need to be considered for any line emission feature.

The degree to which the Ge and Sc layers intermix does not significantly affect the resulting ionization distributions due to the similar \bar{Z} of the two species. Synthetic spectra used in the preceding analysis were generated assuming either pure Ge or pure Sc plasmas at the measured ion density. Any mixture of the two at the same total ion density would yield an electron density modified by the mix fraction and the difference between mean ionization states \bar{Z} . Any mixing can be recast as a constant multiplicative error in the electron density assumed in the kinetics calculation. Furthermore, Ge and Sc each exhibit similar mean ionization states ($\bar{Z}_{Sc} \approx 22$, $\bar{Z}_{Ge} \approx 29$), resulting in a multiplicative error in the electron density of at most 15%. As noted previously, an error in the absolute density does not affect our conclusions.

B. Time-dependent ionization kinetics

We now consider the possibility of a time-dependent ionization of either Sc or Ge and its impact on the inferred temperatures. The ionization of a species must be treated as time-dependent when the ionization equilibration time τ exceeds the fastest thermodynamic time scale $\left[\tau_{hydro} = \left(\frac{1}{n_i}\frac{dn_i}{dt}\right)^{-1}\right]$ or

 $\tau_{th} = \left(\frac{1}{T_e}\frac{dT_e}{dt}\right)^{-1}$. We can estimate τ from a simplified system consisting of the ground states of two charge states Z and Z+1. (This approximation is exact for H in the low-density coronal limit.) Neglecting excited states, the two charge states are connected by collisional ionization and radiative recombination with respective rate coefficients S and α . Conservation of particles allows definition of the total ion density $n_i = n_Z + n_{Z+1}$ and free electron density $n_e = \bar{Z}n_i$. Solution of the corresponding rate equation

$$\frac{d\mathbf{n}_{\mathbf{Z}}}{dt} = \mathbf{n}_{\mathbf{e}}[\alpha \mathbf{n}_{\mathbf{i}} - (\alpha + S)\mathbf{n}_{\mathbf{Z}}] \tag{2}$$

yields the time-dependent population of the recombined state

$$n_{Z}(t) = \frac{\alpha}{\alpha + S} n_{i} + Ce^{-n_{e}(\alpha + S)t}, \qquad (3)$$

where C is a constant whose value depends on the populations at t = 0. From this we define the equilibration time

$$\tau = \left(n_{e}(\alpha + S) \right)^{-1}. \tag{4}$$

We can evaluate τ for the potential limiting ionization and recombination processes in our system. For Sc, we are concerned that the Sc ionization lags the steady-state value during the heating process, leading to $T_Z^{Sc} < T_e$. Since the observed Sc spectrum is predominantly He-like and the steady-state ionization is anticipated to be further ionized, we will evaluate τ between He-like and H-like Sc. For Ge, likewise, we are concerned that the ionization lags the steady-state value as the plasma expands. A predominant Li-like charge state of Ge and a steady-state ionization that recombines with decreasing density indicates that the recombination of Li-like to Be-like Ge could limit this system.

The calculated ionization and thermodynamic time scales are shown in Fig. 8. S and α are taken from the OPEN-ADAS database. ²⁵ Rate coefficients for Zn are used as a proxy for Ge because the rate coefficients for Ge were unavailable. Due to the atomic-number scaling of the rate coefficients, $\tau_{Zn} > \tau_{Ge}$ and serves as an upper bound for Ge. Probability distributions of the derived time scales were calculated using Monte Carlo error propagation. ²⁶ The corresponding uncertainties are represented by the 90% highest-density interval (HDI) in Fig. 8. Synthetic density datasets are generated by sampling from the product of two Gaussian distributions $G(\mu, \sigma)$ with means μ and standard deviations σ corresponding to the random and systematic uncertainties:

$$n_{jk} = G_{jk}(n(t_j), 0.02 \times n(t_j)) G_k(1, 0.19),$$
 (5)

where n_{jk} is the synthetic ion density at time t_j of the k^{th} synthetic dataset, and the subscript i has been omitted for clarity. The Gaussian distribution G_{jk} accounts for the 2% random uncertainty in the individual measurements and is evaluated for each of the $N_j \times N_k$ synthetic measurements. The Gaussian distribution G_k accounts for the fractional systematic uncertainty of the unknown buried layer mass and is evaluated once for each of the N_k synthetic datasets. A larger systematic uncertainty of 19% is used to incorporate shot-to-shot variability in n_i . Because uncertainties in T_Z are not divisible into

random and systematic sources, T_Z of Sc and Ge are fit with separate sigmoid functions

$$T_Z(t) = A (1 + e^{-(t-B)/C})^{-1}$$
 (6)

using Bayesian inference. 27,28 Synthetic temperatures are sampled from the resulting posterior predictive distributions. Distributions of the τ are calculated from the T_e and n_i samples and are used to determine the HDI's.

The ionization of both Ge and Sc begin in steady-state due to the higher density and shorter ionization time scales early during the expansion. Because measurements were performed once the temperature approached a steady-state, τ_{th} is the longest time scale for all times. Temperature does not impact the time-dependence of the system. As the plasma expands, $\tau_{hydro} < \tau_{Sc}$ for t > 2.4 ns, suggesting that the Sc ionization will not equilibrate with the evolving plasma conditions. If the plasma temperature T_e continues to increase while $\tau_{Ge} < \tau_{hydro} < \tau_{Sc}$, a situation will arise where $T_Z^{Sc} < T_Z^{Ge}$, consistent with the inferred T_Z for these times. Ge, having a faster τ , will exhibit an ionization that follows T_e more closely than that of Sc. Because no independent measurement of T_e was made, we cannot conclusively determine the relationship between T_e and T_Z^{Ge} or the time-dependence of the Ge ionization.

As an additional check of the time-dependence, we have performed time-dependent calculations of the atomic state populations and resulting spectra using SCRAM. Timedependent calculations of the Ge spectra using $T_Z^{Ge}(t)$ closely resemble the corresponding steady-state calculations. According to these calculations, it is unlikely that the Ge ionization is time-dependent. Time-dependent calculations of the Sc spectra were performed for $T_7^{Ge}(t)$. The calculations indicate a departure from steady state but fail to reproduce the observed Sc spectra. The calculated time-dependent ionization is too slow, and the Ly α intensity is lower than observed for all but the latest time. However, Fig. 8 indicates that the Ge ionization may also become time-dependent after 2.6 ns, in which case T₇^{Ge} becomes an inaccurate diagnostic of T_e. To determine a $T_e - n_i$ trajectory consistent with all measurements, the time-dependent Sc and Ge spectra would need to be generated along an ensemble of plausible $T_e - n_i$ trajectories and analyzed for goodness of fit to the observed Ge and Sc spectra. Such multi-dimensional, multi-objective optimization is beyond the scope of this paper.

V. CONCLUSION

The development of accurate non-LTE atomic spectral models relies on experimental spectra from a characterized source. Few datasets exist in the literature due to the difficulty of creating and diagnosing non-LTE plasmas. We have presented simultaneous Sc K-shell and Ge L-shell spectra from an expanding buried-layer plasma with a measured ion density. The two spectra not only serve as a stringent test of spectral models but also provide an *in-situ* determination of ionization equilibrium. Sc K-shell and Ge L-shell spectra obtained during the early-phase expansion are successfully reproduced by a steady-state calculation by the atomic kinetics

model SCRAM at the measured density and a single temperature. This demonstrates the accuracy of the atomic kinetics model within SCRAM. As the plasma expands, steady-state calculations fail to match both spectra at the same plasma conditions. We find that $T_Z^{Ge} > T_Z^{S\bar{c}}$. Calculations of the thermodynamic and ionization time scales throughout the experiment suggest that the Sc ionization departs from steady state between 2.3 and 2.5 ns, prior to Ge's potential departure from steady state around 2.6 ns. The difference in T_Z is thus most likely due to a time-dependent ionization state of Sc while the plasma temperature rises. The Sc spectra underestimates the plasma temperature, resulting in the observed $T_Z^{Ge} > T_Z^{Sc}$. Time-dependent SCRAM calculations were unable to reproduce both spectra but may require an exhaustive search of parameter space to find a thermodynamic path consistent with all measurements.

Rather than signaling the end of a useful measurement, the onset of time-dependence of the Sc ionization poses an important observation for atomic kinetics models to reproduce. The thermodynamic time scales can be experimentally varied to force disequilibrium to occur earlier or later during the experiment to further test the accuracy of kinetics models. Additionally, time-dependent ionization increases the complexity of K-shell temperature diagnostics in expanding plasmas. The possibility of such must be considered carefully when using ionization-based plasma diagnostics at low densities.

ACKNOWLEDGMENTS

This material is based upon work supported by the Department of Energy National Nuclear Security Administration under Award Number DE-NA0003856, the University of Rochester, and the New York State Energy Research and Development Authority, and under the auspices of the U.S. Department of Energy by Lawrence Livermore National Laboratory under Contract DEAC52-07NA27344. D.A.C. acknowledges the DOE NNSA SSGF support, which is provided under Cooperative Agreement No. DE-NA0003960

This report was prepared as an account of work sponsored by an agency of the U.S. Government. Neither the U.S. Government nor any agency thereof, nor any of their employees, makes any warranty, express or implied, or assumes any legal liability or responsibility for the accuracy, completeness, or usefulness of any information, apparatus, product, or process disclosed, or represents that its use would not infringe privately owned rights. Reference herein to any specific commercial product, process, or service by trade name, trademark, manufacturer, or otherwise does not necessarily constitute or imply its endorsement, recommendation, or favoring by the U.S. Government or any agency thereof. The views and opinions of authors expressed herein do not necessarily state or reflect those of the U.S. Government or any agency thereof.

- ⁴S. B. Hansen, H. K. Chung, C. J. Fontes, Y. Ralchenko, H. A. Scott, and E. Stambulchik, High Energy Density Phys. **35**, 100693 (2020), arXiv:1903.09605.
- ⁵R. F. Heeter, S. B. Hansen, K. B. Fournier, M. E. Foord, D. H. Froula, A. J. MacKinnon, M. J. May, M. B. Schneider, and B. K. Young, Phys. Rev. Lett. **99**, 1 (2007).
- ⁶M. J. Herbst, P. G. Burkhalter, J. Grun, R. R. Whitlock, and M. Fink, Rev. Sci. Instrum. 53, 1418 (1982).
- ⁷P. G. Burkhalter, M. J. Herbst, D. Duston, J. Gardner, M. Emery, R. R. Whitlock, J. Grun, J. P. Apruzese, and J. Davis, Phys. Fluids **26**, 3650 (1983).
- ⁸R. L. Kauffman, R. W. Lee, and K. Estabrook, Phys. Rev. A 35, 4286 (1987).
- ⁹L. Aschke, S. Depierreux, K. G. Estabrook, K. B. Fournier, J. Fuchs, S. Glenzer, R. W. Lee, W. Rozmus, R. S. Thoe, and P. E. Young, J. Quant. Spectrosc. Radiat. Transf. **65**, 23 (2000).
- ¹⁰M. E. Foord, S. H. Glenzer, R. S. Thoe, K. L. Wong, K. B. Fournier, J. R. Albritton, B. G. Wilson, and P. T. Springer, J. Quant. Spectrosc. Radiat. Transf. 65, 231 (2000).
- ¹¹M. E. Foord, S. H. Glenzer, R. S. Thoe, K. L. Wong, K. B. Fournier, B. G. Wilson, and P. T. Springer, Phys. Rev. Lett. 85, 4 (2000).
- ¹²T. D. Shepard, C. A. Back, D. H. Kalantar, R. L. Kauffman, C. J. Keane, D. E. Klem, B. F. Lasinski, B. J. MacGowan, L. V. Powers, L. J. Suter, R. E. Turner, B. H. Failor, and W. W. Hsing, Phys. Rev. E 53, 5291 (1996).
- ¹³D. M. Chambers, P. A. Pinto, J. Hawreliak, I. R. Al'Miev, A. Gouveia, P. Sondhauss, E. Wolfrum, J. S. Wark, S. H. Glenzer, R. W. Lee, P. E. Young, O. Renner, R. S. Marjoribanks, and S. Topping, Phys. Rev. E 66, 1 (2002).
- ¹⁴E. V. Marley, D. A. Liedahl, M. B. Schneider, R. F. Heeter, L. C. Jarrott, C. W. Mauche, G. E. Kemp, M. E. Foord, Y. Frank, K. Widmann, and J. Emig, Rev. Sci. Instrum. 89, 1 (2018).
- ¹⁵S. B. Hansen, Development and Application of L-Shell Spectroscopic Modeling for Plasma Diagnostics, Ph.D. thesis, University of Nevada, Reno (2003).
- ¹⁶The sense in which we mean "equilibrium" is "thermal equilibrium between a species' ionization distribution and the free electrons in the circumfluent plasma".
- ¹⁷J. D. Kilkenny, Laser Part. Beams **9**, 49 (1991).
- ¹⁸M. May, R. Heeter, and J. Emig, Rev. Sci. Instrum. **75**, 3740 (2004).
- ¹⁹R. F. Heeter, J. A. Emig, K. B. Fournier, S. B. Hansen, M. J. May, and B. K. Young, Rev. Sci. Instrum. **75**, 3762 (2004).
- ²⁰R. E. Marrs, G. V. Brown, J. A. Emig, and R. F. Heeter, Rev. Sci. Instrum. 85 (2014), 10.1063/1.4892552.
- ²¹G. Pérez-Callejo, D. A. Liedahl, M. B. Schneider, S. J. Rose, and J. S. Wark, High Energy Density Phys. (2019), 10.1016/j.hedp.2019.01.005.
- ²²G. Pérez-Callejo, L. C. Jarrott, D. A. Liedahl, E. V. Marley, G. E. Kemp, R. F. Heeter, J. A. Emig, M. E. Foord, K. Widmann, J. Jaquez, H. Huang, S. J. Rose, J. S. Wark, and M. B. Schneider, Phys. Plasmas **26** (2019), 10.1063/1.5096972.
- ²³G. Pérez-Callejo, E. V. Marley, D. A. Liedahl, L. C. Jarrott, G. E. Kemp, R. F. Heeter, J. A. Emig, M. E. Foord, M. B. Schneider, S. J. Rose, and J. S. Wark, Phys. Rev. Lett. **126**, 1 (2021).
- ²⁴Y. Frank, G. E. Kemp, E. V. Marley, G. P. Callejo, M. E. Foord, M. B. Schneider, Y. Ehrlich, and M. Fraenkel, Phys. Plasmas 27, 063301 (2020).
 ²⁵"OPEN-ADAS,".
- ²⁶A. Possolo and H. K. Iyer, Rev. Sci. Instrum. **88** (2017), 10.1063/1.4974274.
- ²⁷D. Sivia and J. Skilling, *Data Analysis: A Bayesian Tutorial*, 2nd ed. (Oxford Science Publications, Oxford, United Kingdom, 2012).
- ²⁸E. Bingham, J. P. Chen, M. Jankowiak, F. Obermeyer, N. Pradhan, T. Karaletsos, R. Singh, P. Szerlip, P. Horsfall, and N. D. Goodman, J. Mach. Learn. Res. 20, 1 (2019), arXiv:1810.09538.
- ²⁹R. D. Cowan, *The Theory of Atomic Structure and Spectra*, Los Alamos series in basic and applied sciences (University of California Press, Berkeley, 1081)
- ³⁰S. B. Hansen, J. Bauche, C. Bauche-Arnoult, and M. F. Gu, High Energy Density Phys. (2007), 10.1016/j.hedp.2007.02.032.
- ³¹R. L. Kauffman, R. W. Lee, D. L. Matthews, and J. D. Kilkenny, J. Quant. Spectrosc. Radiat. Transf. 32, 335 (1984).
- ³²H. R. Griem, *Principles of Plasma Spectroscopy*, edited by M. G. Haines,

¹H. K. Chung and R. W. Lee, High Energy Density Phys. **5**, 1 (2009).

²H. A. Scott and S. B. Hansen, High Energy Density Phys. **6**, 39 (2010).

³R. Piron, F. Gilleron, Y. Aglitskiy, H. K. Chung, C. J. Fontes, S. B. Hansen, O. Marchuk, H. A. Scott, E. Stambulchik, and Y. Ralchenko, High Energy Density Phys. **23**, 38 (2017).

K. I. Hopkraft, I. H. Hutchinson, C. M. Surko, and K. Schindler (Cam-

bridge University Press, New York, 2005).

³³R. McWhirter, in *Plasma Diagnostics Tech.*, edited by Richard H. Huddlestone and S. L. Leonard (Academic Press, New York, 1965) Chap. 5, pp. 201–264. ³⁴B. K. Young, R. E. Stewart, C. J. Cerjan, G. Charatis, and G. E. Busch, Phys. Rev. Lett. **61**, 2851 (1988). ³⁵J. A. van der Mullen, Phys. Rep. **191**, 109 (1990).